

# **Routers of valley excitons in a WS<sub>2</sub> monolayer via delocalized Bloch modes of in-plane inversion-symmetry broken photonic crystal slabs**

Jiajun Wang<sup>1,\*</sup>, Han Li<sup>2,\*</sup>, Yating Ma<sup>2</sup>, Maoxiong Zhao<sup>1</sup>, Wenzhe Liu<sup>1</sup>, Bo Wang<sup>1</sup>, Shiwei Wu<sup>1,3</sup>, Xiaohan Liu<sup>1,3</sup>, Lei Shi<sup>1,3,†</sup>, Tian Jiang<sup>2,‡</sup>, and Jian Zi<sup>1,3,§</sup>

<sup>1</sup> State Key Laboratory of Surface Physics, Key Laboratory of Micro- and Nano-Photonics Structures (Ministry of Education) and Department of Physics, Fudan University, Shanghai 200433, China

<sup>2</sup> College of Advanced Interdisciplinary Studies, National Universities of Defense Technology, Changsha 410073, China

<sup>3</sup> Collaborative Innovation Center of Advanced Microstructures, Nanjing University, Nanjing 210093, China

\* These authors contributed equally to this work.

† lshi@fudan.edu.cn

‡ tjjiang@nudt.edu.cn

§ jzi@fudan.edu.cn

## Abstract

The valleys of two-dimensional transition metal dichalcogenides (TMDCs) offer a new degree of freedom for information processing. To take advantage of this valley degree of freedom, on one hand, it is feasible to control valleys by utilizing different external stimuli like optical and electric fields. On the other hand, nanostructures are also used to separate the valleys by near field coupling. However, for both above methods, either required low-temperature environment or low degree of coherence properties limit their further applications. Here, we demonstrate all-dielectric photonic crystal (PhC) slabs with in-plane inversion symmetry ( $C_2$  symmetry) broken could serve as routers of valley excitons in a  $WS_2$  monolayer at room temperature. Coupling with circularly polarized photonic Bloch modes of such PhC slabs, valley photons emitted by a  $WS_2$  monolayer are routed directionally and efficiently separated in far field. In addition, the far-field emission is significantly enhanced and with long-distance spatial coherence property. Our work paves the way for developing room-temperature valleytronics, extending its potential applications in remote wireless information processing.

## Introduction

The emergence of two-dimensional transition metal dichalcogenides (TMDCs) has attracted tremendous interest for their possible applications in valleytronics<sup>1–11</sup>. Due to the broken inversion symmetry in TMDCs, two degenerates yet inequivalent valleys (labeled as K and K' valleys) appear at the corners of the first Brillouin zone, shown in Fig. 1a. Together with the strong spin-orbital interaction, opposite spin splitting occurs in two valleys of TMDCs, resulting in spin-valley locking<sup>1–4</sup>. Hence, interband transitions at two valleys, which are excitonic in nature for TMDCs, show highly valley-dependent optical selection rules<sup>12–14</sup>. This controllable selective population of certain valleys, called valley polarization, offers a new degree of freedom based on valleys of TMDCs. This valley degree of freedom has been considered as new kind of information carriers, spawning an emergent field of valleytronics<sup>15–19</sup>. In valleytronics devices, as the exclusive coupling of the valley excitons to the handedness of circularly polarized light, optical operation of the valley degree of freedom is feasible and of vital importance. Meanwhile, if the emission from inequivalent valley excitons could be separated in far field, valleytronics would also be suitable for remote wireless information processing applications. Thus, a router as an interface of valley excitons and photons is highly desired to guide different handedness of circularly polarized emission light carrying valley polarization information to different directions in far field.

Due to the powerful ability of manipulating light, optical nanoantennas<sup>20</sup> and metasurfaces<sup>21–23</sup> are usually proposed to direct emission from opposite valleys into different directions<sup>24–33</sup>. To be specific, photonic spin Hall effect based on either transverse spin momentum of surface plasmons<sup>25,26</sup> or geometric phase given by spatial variable nanoantennas<sup>27</sup>, is applied to separate valley excitons' emission with different chirality. Similar phenomenon could also be achieved by using multipolar interference of complex asymmetric single nanoantenna. However, both the intrinsic loss of metal materials and the localized spatial distribution of resonant modes of nanoantennas limit the efficient directional emission of valley photons, leading to low degree of valley polarization in far field<sup>26,29–31</sup>. To realize high degree of valley polarization in far field, it should be pointed out that in fact the spatial coherence properties of the emission of valley excitons in near field play a vital role, which are neglected

to be discussed in the past studies. For this reason, photonic structures with high degree of spatial coherence properties are required, and we find all-dielectric photonic crystal (PhC) slabs could be a suitable system. As a counterpart of metasurfaces, photonic crystal slabs are also widely used to control light interaction<sup>34–37</sup>. Comparing to metasurfaces based on local resonances of nanoantennas, PhC slabs are based on a series of delocalized photonic Bloch modes with different frequencies and wavevectors, forming photonic band structures in momentum space<sup>36, 37</sup>. Notably, the delocalized nature of those Bloch modes ensures the possible applications in coherent emission<sup>38, 39</sup>. Meanwhile, different from metasurfaces, PhC slabs are not limited to metal or high refractive index materials. That means low intrinsic loss in visible frequency range could be realized in many available dielectric materials, which could directly enhance the radiation efficiency. Moreover, besides the applications on realization of coherent light emission, PhC slabs can also be applied in polarization manipulation. And recently we have reported that in far field, the polarization states of each Bloch modes can cover entire Poincaré sphere<sup>40</sup>(a space to describe all polarization states, shown in Fig. 1b). Full-covered Poincaré sphere, especially with two poles (circularly polarized states with opposite chirality), as well as the pre-mentioned delocalized spatial distribution of Bloch modes, offers an ideal platform to control the emission of valley photons.

In this article, we demonstrate that two-dimensional all-dielectric photonic crystal slabs with in-plane inversion symmetry broken can be used to route the directional emission of valley photons in a WS<sub>2</sub> monolayer to far field at room temperature with high efficiency, high degree of valley polarization and long spatial coherence length, as shown in Fig. 1d. Paired photonic Bloch modes with different circular polarization are important to separate and enhance directional emission of valley photons. Experimentally, the angle-resolved photoluminescence (PL) results show that the degree of valley polarization yields the maximum to 88%. The double-slit interference results characterize that the spatial coherence length of emission field on WS<sub>2</sub> monolayer is longer than 6 microns (29 microns in theory). Therefore, our results show that photonic crystal slabs could be designed to serve as routers of valley photons at room temperature, extending valleytronic devices to wireless information processing applications.

## Results and Discussion

Analogous to electronic band structures in solids, the Bloch scattering by periodic artificial atoms of PhC slabs alters the dispersion relation of light in the slab, resulting in photonic bands. Each optical state in photonic bands corresponds to the delocalized Bloch mode with well-defined energy and momentum, reflecting high degree of temporal and spatial coherence properties. Modes above the light cone are radiative due to coupling to the free space<sup>37,41</sup>. For these radiative modes, their polarization states in far field are strictly defined. And the corresponding polarization states of radiative Bloch modes in an arbitrary photonic band could be further projected into the structure plane and mapped onto the Brillouin zone, defining a polarization field in momentum space<sup>42,43</sup>. The polarization field could define vortex singularities in momentum space such as bound states in the continuum (BICs), offering a new view of singular optics in photonic crystal's research<sup>43–47</sup>. Such singularities could be applied in research of light-matter interaction such as developing BIC laser<sup>48</sup>. Besides vortex singularities, the polarization property of single photonic mode in principle could be used in controlling the radiation of luminescent material. However, owing to high rotation symmetry,

the polarization field is nearly linear in most PhC slabs<sup>49</sup>. As a consequence, the polarization states of those PhC slabs could only cover a belt near the equator of the Poincaré sphere. With a large area including two poles not covered, it is useless for us to utilize these Bloch modes of PhC slabs to separate the valley photons in TMDCs.

On the contrary, as we know, the broken inversion symmetry is of vital importance in the appearance of inequivalent valley excitons in TMDCs. And inspired by this fact, similar principle could also be applied in PhC slabs for generating opposite circularly polarized radiative states in the momentum space. In our recent work, it is reported that paired circularly polarized states (circular singularities in singular optics) with different chirality would spawn from vortex singularities after breaking the in-plane inversion symmetry of PhC slabs (shown in Fig. 1c). Therefore, besides the areas near the equator, the polarization states cover the whole sphere including two poles of the Poincaré sphere, corresponding to polarization states with high degree of circular polarization in momentum space. Therefore, this type of PhC slabs with circularly polarized radiative states could be an ideal platform for us to separate valley photons of TMDCs in far field (shown in Fig. 1d). Firstly, valley photons could couple to circularly-polarized states with corresponding chirality and get separated in momentum space. Secondly, as we mentioned, these Bloch modes are delocalized and could be used in coherent emission[38, 39]. The spatial coherence properties of the emission field lay the foundation for high-efficient separation of valley excitons in a WS<sub>2</sub> monolayer and the application as a router. Detailed discussion is provided in Supplementary Material section 1.

To demonstrate the existences of the opposite circularly polarized states in momentum space, we designed an in-plane inversion-symmetry broken PhC slab and studied the transmittance spectra in theory and experiment, shown in Fig. 2. The slabs here are made of silicon nitride (Si<sub>3</sub>N<sub>4</sub>, refractive index  $\sim 2$ ) and silicon dioxide (SiO<sub>2</sub>, refractive index  $\sim 1.5$ ). The thickness of Si<sub>3</sub>N<sub>4</sub> layer is 150 nm. And the thickness of SiO<sub>2</sub> layer is 500 microns, which could be considered infinite compared to the wavelength of visible light. Square lattices of holes with a period  $a = 390$  nm are etched in the Si<sub>3</sub>N<sub>4</sub> layer. To break the in-plane inversion symmetry, the shape of the etched hole in a unit cell is set as an isosceles triangle, with the height  $h$  and the baseline length  $b$  of the triangle being equal ( $h = b = 250$  nm), shown in Fig. 2a.

We first simulated the angle-resolved transmittance spectra under  $\sigma_+$  polarized incidence by Rigorous Coupled Wave Analysis (RCWA), with the incidence plane along  $\Gamma$ -X direction. The spectra are asymmetric and there are some diminished regions on the photonic bands, pointed out by blue arrows in Fig. 2b. These diminished regions correspond to the nonexcited states under  $\sigma_+$  polarized incidence. Hence those states in the diminished regions are  $\sigma_-$  polarized. Changing the incident light to  $\sigma_-$  polarization, the diminished regions switch to the other side (Fig. S1a). To show it experimentally, we fabricated samples using electron-beam lithography and reactive ion etching (for more details see Methods). By using homemade polarization-resolved momentum-space imaging spectroscopy system (Fig. S2), angle-resolved transmittance spectra are measured (Fig. 2c), in accordance with the simulation. Both simulated and experimentally measured results confirmed the appearance of optical modes with high degree of circular polarization in our designed PhC slab. For comparison, we also researched the angle-resolved transmittance spectra of the PhC slab with in-plane inversion symmetry. Shown in Fig. 2d, the designed shape of etched hole in the unit is a circle (diameter  $d = 210$  nm). As expected, we did not observe the asymmetric spectra under  $\sigma_+$  polarized incidence both

in simulation and experiment, shown in Fig. 2e-f. When changing the incidence to  $\sigma$ -polarization, the transmittance spectra is the same as the case of  $\sigma_+$  polarization (Fig. S1b). The results demonstrate that by breaking in-plane inversion symmetry of PhC slabs, circularly polarized states would emerge in photonic bands.

The large area of  $\text{WS}_2$  monolayer, shown representatively in Fig. 3a, is grown on Si/SiO<sub>2</sub> substrate by CVD process and then transferred onto PhC slabs (for details see Methods). Both PhC slabs and part of unstructured flat Si<sub>3</sub>N<sub>4</sub> substrate are covered. Different outline colors refer to  $\text{WS}_2$  monolayer on different substrates. Red (orange) corresponds to PhC slab etched triangle (circle) holes, and blue corresponds to flat substrate. We take photoluminescence (PL) spectra using a linearly polarized laser centered at 532 nm at room temperature (Fig. 3a). The PL intensity is enhanced when  $\text{WS}_2$  monolayer is placed on PhC slabs in contrast with flat substrate. Specially, PL on the PhC slab with in-plane inversion symmetry broken is enhanced most. Then, we performed time-resolved PL measurement at room temperature (for details see Method). Compared with  $\text{WS}_2$  monolayer on a flat substrate, the exciton radiative rate, namely reciprocal of radiative lifetime, is enhanced 75% when  $\text{WS}_2$  monolayer is on PhC slab with in-plane inversion symmetry broken, in accordance with the PL results.

To study the PL distribution in far field, angle-resolved PL spectra are measured, shown in Fig. 3b-i. The detection plane is along  $\Gamma$ -X direction, in accordance with transmittance spectra measurement in Fig. 2. We selected the  $\sigma_+$  ( $\sigma_-$ ) PL by placing a quarter-wave plate and a linear polarizer in the detection path (Fig. S2). Fig. 3f-g show the asymmetric  $\sigma_+$  ( $\sigma_-$ ) PL spectra of  $\text{WS}_2$  monolayer on the PhC slab with in-plane inversion symmetry broken. The  $\sigma_+$  ( $\sigma_-$ ) PL enhanced regions correspond to regions with high degree of  $\sigma_+$  ( $\sigma_-$ ) polarization in photonic bands. Fig. 3b-c show  $\sigma_+$  ( $\sigma_-$ ) PL spectra of  $\text{WS}_2$  monolayer on a flat substrate. And Fig. 3d-e show  $\sigma_+$  ( $\sigma_-$ ) PL spectra of  $\text{WS}_2$  monolayer on the PhC slab with in-plane inversion symmetry. Different from Fig. 3f-g, all spectra in Fig. 3b-e are symmetric for both  $\sigma_+$  and  $\sigma_-$  detection. From the experimental results above, we can draw the conclusion that, as shown in the asymmetric spectra, valley photons emitted by  $\text{WS}_2$  monolayer have been separated in far field by PhC slabs with in-plane inversion symmetry broken.

To further study the degree of separation in Fig. 3f-g, we plotted the angle-resolved  $\sigma_+$  ( $\sigma_-$ ) PL spectra for a single wavelength, shown in Fig. 3h-i. Dot line refers to 615 nm and solid line refers to 628 nm, which are also marked in Fig. 3f-g. We observed that  $\sigma_+$  (red) and  $\sigma_-$  (blue) PL maximums separately appear in different angles. The  $\sigma_+$  and  $\sigma_-$  PL peaks separate nearly 6 degrees at 615 nm and 3 degrees at 627 nm. For comparison, PL spectra on PhC with in-plane inversion symmetry for corresponding wavelengths are shown in Fig. S3, with the  $\sigma_+$  and  $\sigma_-$  PL maximums overlapping in the same angle. We also exhibit the photoluminescence of  $\text{WS}_2$  monolayer on this PhC slab with in-plane inversion symmetry broken is highly directional. Shown in Fig. 3h-i, the full width at half maximum of PL peaks ( $\Delta\theta$ ) is less than 3 degrees at 615 nm and 2 degrees at 627 nm. And this is due to the delocalized property of Bloch modes, leading to long-distance spatial coherence property of the far-field emission by  $\text{WS}_2$  monolayer on PhC slabs. According to the Fourier relation between momentum and position, wide distribution in the real space means that the mode is localized inside a small area in the momentum space. This corresponds to the small angle distribution of the far-field emission, i.e. the directional emission, and will be further discussed later in this article. For this reason, although the separation of  $\sigma_+$  and  $\sigma_-$  PL peaks is small, the valley photons could still be

efficiently separated in far field. Further, we quantify the degree of valley polarization by

$$P(\theta) = \frac{I_+(\theta) - I_-(\theta)}{I_+(\theta) + I_-(\theta)}$$

,where  $I_+$  ( $I_-$ ) refers to the PL intensity with  $\sigma_+$  ( $\sigma_-$ ) polarization for a single wavelength, and  $\theta$  is the radiation angle. The valley polarization is plotted in Fig. S4, with maximum valley polarization calculated up to 84%. These results indicate the PL of WS<sub>2</sub> monolayer on PhC slab with in-plane inversion symmetry broken is highly directional and with high degree of valley polarization.

Basing on the measured angle-resolved  $\sigma_+$  ( $\sigma_-$ ) PL spectra of WS<sub>2</sub> monolayer on PhC slab with in-plane inversion symmetry broken, we mapped the PL intensity distribution of a single wavelength in momentum space, shown in Fig. 4a-d. The upper (lower) row corresponds to 615 (628) nm. The PL spectra along different directions in momentum space were measured by rotating the sample in plane relative to the entrance slit of the imaging spectrometer. And the projected momentum  $k$  is calculated by  $k = k_0 \sin \theta$  ( $k_0 = 2\pi/\lambda$  is the wavevector of light in the free space,  $\theta$  is the emission angle relative to normal of sample plane). The intensity distribution of  $\sigma_+$  ( $\sigma_-$ ) PL in momentum space confirmed that the PhC slab with in-plane inversion symmetry broken leads to directional emission of valley photons.

Then, we used  $P(k)$  to qualify the valley polarization in momentum space, which is similarly defined by  $P(k) = \frac{I_+(k) - I_-(k)}{I_+(k) + I_-(k)}$ , shown in fig. 4e-f. Here,  $I_+$  ( $I_-$ ) refers to the PL intensity with  $\sigma_+$  ( $\sigma_-$ ) polarization for a single wavelength. Experimentally, the maximum  $P$  calculated is up to 88%, obtained in Fig. 4f. Note that, the maximum  $P$  did not appear along the  $\Gamma$ -X direction in momentum space. The result is as expected for the circular polarized states of the designed PhC slab with in-plane inversion symmetry broken are slightly shifted from the  $\Gamma$ -X direction in momentum space<sup>40</sup>. The sign of  $P(k)$  reverses at opposite sides of momentum space, demonstrating the separation of valley photons with different chirality. In contrast, we also measured and calculated  $P(k)$  of the emission by WS<sub>2</sub> monolayer placed on a flat substrate, with  $P(k)$  being negligible (Fig. S5).

In addition to valley-related directional emission in momentum space, we have expected the spatial coherence property of emission by WS<sub>2</sub> monolayer on PhC slab with in-plane inversion symmetry broken. The Young's double-slit experiments were performed, shown in Fig. 5. The experimental setup is illustrated in Fig. 5a. The working principle is based on Fourier transformation, and detailed discussion is provided in Supplementary Material section 3. The double slit is mounted on the real image plane inside the optical measurement setup and the detection plane is along  $\Gamma$ -X direction. Changing the etched depth of PhC slab, we were able to overlap the measured photonic band with the PL spectra of WS<sub>2</sub> monolayer, so that we could obtain enough signal intensity. Interference fringes are observed in the angle-resolved PL spectra, shown in Fig. 5b. The red-marked line is further plotted in Fig. 5c, showing the interference intensity distribution at 621 nm. We mentioned that the double-slit distance is 6 microns, almost ten times the emission wavelength, demonstrating that the measured spectral coherence length is larger than 6 microns. Moreover, the spectral coherence length could be calculated by  $\frac{\lambda}{\Delta\theta}$  in theory, which is widely used in the optical coherence theory<sup>50</sup>. Here,  $\Delta\theta$  is about 0.0215 (1.23° in degree) at 621 nm (Fig. S6), and the calculated spectral coherence length

are around 29 microns. In comparison, no interference fringes are observed when WS<sub>2</sub> monolayer is placed on a flat substrate, as shown in Fig. 5b-c. This means that the far-field emission of WS<sub>2</sub> monolayer on a flat substrate has no long-distance spatial coherence property. Hence, we reveal that the far-field emission by WS<sub>2</sub> monolayer on PhC slab with in-plane inversion symmetry broken has long-distance spatial coherence property. This property of PhC slab extends the coherence control on PL of WS<sub>2</sub> monolayer from temporal coherence to spatial coherence.

In summary, we proposed the in-plane inversion-symmetry broken all-dielectric photonic crystal slabs to route the far-field emission of valley photons of WS<sub>2</sub> monolayer at room temperature. By breaking the in-plane inversion symmetry of PhC slab, we observed paired circularly polarized states with different chirality spawn from vortex singularities. Via coupling with those delocalized Bloch modes, valley photons emitted by WS<sub>2</sub> monolayer were separated in momentum space, and the exciton radiative rate is significantly enhanced. Besides, both the directional emission and the long-distance spatial coherence properties benefit the applications of in-plane inversion-symmetry broken photonic crystal slabs to work as routers of valley photons. In addition, our method could be extended to manipulate valley photons of other TMDCs monolayers. Our work promotes the application of all-dielectric photonic slabs in radiation control of ultra-thin materials and pave the way for developing valley photons routers.

## Methods

**Sample fabrication.** *The fabrication of photonic crystal slab.* The samples' structure was two layers of slab, with a thin silicon nitride layer on the silicon dioxide substrate. The silicon dioxide substrate was cut from a 500-microns-thick quartz wafer. Then a silicon nitride layer was grown on silicon dioxide substrate by plasma-enhanced chemical vapor deposition (PECVD). The thickness of the grown silicon nitride layer was nearly 150 nm and the thickness could be tunable by controlling the deposition time. To fabricate the designed structure, the raw sample was spin-coated with a layer of positive electron beam resist (PMMA950K A4) and an additional layer of conductive polymer (AR-PC 5090.02). Then hole array mask pattern was fabricated onto the PMMA layer using electron beam lithography (ZEISS sigma 300). The sample was further processed by reactive ion etching (RIE). Anisotropic etching was achieved by RIE using CHF<sub>3</sub> and O<sub>2</sub>. The patterned PMMA layer acted as a mask and was eventually removed by RIE using O<sub>2</sub>. The size of every designed structure is approximately 80 × 80 microns.

*Transfer process for WS<sub>2</sub> monolayer.* The CVD WS<sub>2</sub> monolayer on Si/SiO<sub>2</sub> substrate was spin-coated with poly (L-lactic acid) (PLLA) before baking for 5 minutes at 70°C. Afterwards, a PDMS elastomer was placed on top of PLLA film and then torn off. The composite was then attached to a glass slide and put under the microscope on a transfer stage. The PhC slab placed under the glass slide was aligned carefully using microscope and the glass slide was lowered to contact PhC slab. The stage was heated to 70°C to improve the adhesion, then the glass slide was lifted with PDMS on it, leaving WS<sub>2</sub> monolayer on the PhC slabs. After dissolving PLLA in dichloromethane, the WS<sub>2</sub> monolayer was finally transferred to designed photonic crystal slabs.

**Optical measurements.** *Measurement setup of the polarization-resolved momentum-space imaging spectroscopy system and double-slit experiment.* Please see the supplementary Material for the

schematics and discussions.

*Time-resolved photoluminescence experiment.* Related measurements were finished in a lab-built confocal PL system. By setting the grating to zero order, CCD in spectrometer captured PL image in real space. In TR-PL experiment, both WS<sub>2</sub> on designed PhC slabs and flat substrate were excited under 400 nm laser of 100 fs pulse-width and corresponding TR-PL decay traces were collected by a time-correlated single photon counting (TCSPC) device. After deconvolution of measured decay traces with instrument response function (IRF), TR-PL decay traces were fitted by a biexponential model consisting of non-radiative recombination and radiative recombination processes.

**Simulations.** The transmittance spectra were simulated by Rigorous Coupled Wave Analysis (RCWA). The periodic boundary conditions were applied in x, y direction. The polarization angle was set  $\pi/4$  and phase difference was set  $\pi/2$  or  $3\pi/2$  to get circularly polarized incidence (The polarization angle 0 ( $\pi/2$ ) corresponds to p (s) polarization). The Si<sub>3</sub>N<sub>4</sub> refractive index was set to 2 and SiO<sub>2</sub> refractive index was set to 1.5. All the materials were considered no loss in visible light.

### Acknowledgements

The work was supported by 973 Program and China National Key Basic Research Program (2015CB659400, 2016YFA0301100, 2016YFA0302000 and 2018YFA0306201) and National Science Foundation of China (11774063, 11727811 and 91750102, 11804387, 11802339, 11805276, 61805282, 61801498, and 11902358), and the Youth talent lifting project (Grant No. 17-JCJQ-QT-004). The research of L. S. was further supported by Science and Technology Commission of Shanghai Municipality (17ZR1442300, 17142200100).

### Conflict of interest

The authors declare that they have no conflict of interest.

### Contributions

L. S, T. J, and J. Z conceived the basic idea for this work. J. W designed the structure, performed the sample fabrications, and carried out the RCWA simulations. Y. M performed the material transfer. H. L, J. W and Y. M performed the TR-PL measurement. J. W and M. Z performed the angle-resolved spectra measurement. J. W and H. L analyzed the experimental data. L. S, T. J and J. Z supervised the search and the development of the manuscript. J. W and L. S write the draft of the manuscript. All the authors contributed to the discussion of the results and writing the manuscript.

### Data availability

The data that support the findings of this study are available from the authors on reasonable request, see author contributions for specific data sets.

### References

1. Xiao, D., Yao, W. & Niu, Q. Valley-contrasting physics in graphene: magnetic moment and topological transport. *Phys. Rev. Lett.* **99**, 236809 (2007).
2. Yao, W., Xiao, D. & Niu, Q. Valley-dependent optoelectronics from inversion symmetry breaking. *Phys. Rev. B* **77**, 235406 (2008).



3. Xu, X., Yao, W., Xiao, D. & Heinz, T. F. Spin and pseudospins in layered transition metal dichalcogenides. *Nat. Phys.* **10**, 343 (2014).
4. Cao, T. *et al.* Valley-selective circular dichroism of monolayer molybdenum disulphide. *Nat. Commun.* **3**, 887 (2012).
5. Xiao, J. *et al.* Nonlinear optical selection rule based on valley-exciton locking in monolayer WS<sub>2</sub>. *Light Sci. Appl.* **4**, e366–e366 (2015).
6. Zhu, B., Zeng, H., Dai, J., Gong, Z. & Cui, X. Anomalously robust valley polarization and valley coherence in bilayer WS<sub>2</sub>. *Proc. Natl. Acad. Sci.* **111**, 11606–11611 (2014).
7. Wang, T. *et al.* Giant Valley-Zeeman Splitting from Spin-Singlet and Spin-Triplet Interlayer Excitons in WSe<sub>2</sub>/MoSe<sub>2</sub> Heterostructure. *Nano Lett.* (2019).
8. Li, Z. *et al.* Emerging photoluminescence from the dark-exciton phonon replica in monolayer WSe<sub>2</sub>. *Nat. Commun.* **10**, 2469 (2019).
9. Du, L. *et al.* Giant Valley Coherence at Room Temperature in 3R WS<sub>2</sub> with Broken Inversion Symmetry. *Research* **2019**, 6494565 (2019).
10. Sun, Z., Martinez, A. & Wang, F. Optical modulators with 2D layered materials. *Nat. Photonics* **10**, 227 (2016).
11. Autere, A. *et al.* Nonlinear optics with 2D layered materials. *Adv. Mater.* **30**, 1705963 (2018).
12. Mak, K. F., He, K., Shan, J. & Heinz, T. F. Control of valley polarization in monolayer MoS<sub>2</sub> by optical helicity. *Nat. Nanotechnol.* **7**, 494 (2012).
13. Zeng, H., Dai, J., Yao, W., Xiao, D. & Cui, X. Valley polarization in MoS<sub>2</sub> monolayers by optical pumping. *Nat. Nanotechnol.* **7**, 490 (2012).
14. Sun, Z. *et al.* Optical control of room-temperature valley polaritons. *Nat. Photonics* **11**, 491 (2017).
15. Schaibley, J. R. *et al.* Valleytronics in 2D materials. *Nat. Rev. Mater.* **1**, 16055 (2016).
16. Splendiani, A. *et al.* Emerging photoluminescence in monolayer MoS<sub>2</sub>. *Nano Lett.* **10**, 1271–1275 (2010).
17. Mak, K. F., Xiao, D. & Shan, J. Light–valley interactions in 2D semiconductors. *Nat. Photonics* **12**, 451 (2018).
18. Kim, J. *et al.* Ultrafast generation of pseudo-magnetic field for valley excitons in WSe<sub>2</sub> monolayers. *Science* **346**, 1205–1208 (2014).
19. Lundt, N. *et al.* Optical valley Hall effect for highly valley-coherent exciton-polaritons in an atomically thin semiconductor. *Nat. Nanotechnol.* **14**, 770–775 (2019).
20. Chen, H., Liu, M., Xu, L. & Neshev, D. N. Valley-selective directional emission from a transition-metal dichalcogenide monolayer mediated by a plasmonic nanoantenna. *Beilstein J. Nanotechnol.* **9**, 780–788 (2018).
21. Kapitanova, P. V. *et al.* Photonic spin Hall effect in hyperbolic metamaterials for polarization-controlled routing of subwavelength modes. *Nat. Commun.* **5**, 3226 (2014).
22. Chen, J. *et al.* Tunable and enhanced light emission in hybrid WS<sub>2</sub>-optical-fiber-nanowire structures. *Light Sci. Appl.* **8**, 1–8 (2019).
23. Lin, J. *et al.* Polarization-controlled tunable directional coupling of surface plasmon polaritons. *Science* **340**, 331–334 (2013).
24. Li, Z. *et al.* Tailoring MoS<sub>2</sub> Valley-Polarized Photoluminescence with Super Chiral Near-Field. *Adv. Mater.* **30**, 1801908 (2018).
25. Gong, S.-H., Alpeggiani, F., Sciacca, B., Garnett, E. C. & Kuipers, L. Nanoscale chiral valley-

- photon interface through optical spin-orbit coupling. *Science* **359**, 443–447 (2018).
26. Sun, L. *et al.* Separation of valley excitons in a MoS<sub>2</sub> monolayer using a subwavelength asymmetric groove array. *Nat. Photonics* **13**, 180 (2019).
  27. Hu, G. *et al.* Coherent steering of nonlinear chiral valley photons with a synthetic Au–WS<sub>2</sub> metasurface. *Nat. Photonics* **1** (2019).
  28. Li, Z. *et al.* Tailoring MoS<sub>2</sub> exciton–plasmon interaction by optical spin–orbit coupling. *ACS Nano* **11**, 1165–1171 (2016).
  29. Guddala, S., Bushati, R., Li, M., Khanikaev, A. & Menon, V. Valley selective optical control of excitons in 2D semiconductors using a chiral metasurface. *Opt. Mater. Express* **9**, 536–543 (2019).
  30. Wu, Z., Li, J., Zhang, X., Redwing, J. M. & Zheng, Y. Room-Temperature Active Modulation of Valley Dynamics in a Monolayer Semiconductor through Chiral Purcell Effects. *Adv. Mater.* **31**, 1904132 (2019).
  31. Chervy, T. *et al.* Room temperature chiral coupling of valley excitons with spin-momentum locked surface plasmons. *ACS Photonics* **5**, 1281–1287 (2018).
  32. Chen, P. *et al.* Chiral Coupling of Valley Excitons and Light through Photonic Spin–Orbit Interactions. *Adv. Opt. Mater.* 1901233 (2019).
  33. Krasnok, A. & Alù, A. Valley-selective response of nanostructures coupled to 2D transition-metal dichalcogenides. *Appl. Sci.* **8**, 1157 (2018).
  34. Wu, S. *et al.* Control of two-dimensional excitonic light emission via photonic crystal. *2D Mater.* **1**, 011001 (2014).
  35. Wu, S. *et al.* Monolayer semiconductor nanocavity lasers with ultralow thresholds. *Nature* **520**, 69 (2015).
  36. Joannopoulos, J. D., Villeneuve, P. R. & Fan, S. Photonic crystals. *Solid State Commun.* **102**, 165–173 (1997).
  37. Fan, S. & Joannopoulos, J. D. Analysis of guided resonances in photonic crystal slabs. *Phys. Rev. B* **65**, 235112 (2002).
  38. Carminati, R. & Greffet, J.-J. Near-field effects in spatial coherence of thermal sources. *Phys. Rev. Lett.* **82**, 1660 (1999).
  39. Shi, L. *et al.* Coherent fluorescence emission by using hybrid photonic–plasmonic crystals. *Laser Photonics Rev.* **8**, 717–725 (2014).
  40. Liu, W. *et al.* Circularly polarized states spawning from bound states in the continuum. *Phys. Rev. Lett.* **123**, 116104 (2019).
  41. Wang, J. *et al.* Observation of optical states below the light cone with compound lattices. *OSA Contin.* **2**, 1844–1850 (2019).
  42. Zhen, B., Hsu, C. W., Lu, L., Stone, A. D. & Soljačić, M. Topological nature of optical bound states in the continuum. *Phys. Rev. Lett.* **113**, 257401 (2014).
  43. Zhang, Y. *et al.* Observation of polarization vortices in momentum space. *Phys. Rev. Lett.* **120**, 186103 (2018).
  44. Hsu, C. W. *et al.* Observation of trapped light within the radiation continuum. *Nature* **499**, 188 (2013).
  45. Yang, Y., Peng, C., Liang, Y., Li, Z. & Noda, S. Analytical perspective for bound states in the continuum in photonic crystal slabs. *Phys. Rev. Lett.* **113**, 037401 (2014).
  46. Xiao, Y.-X., Ma, G., Zhang, Z.-Q. & Chan, C. Topological subspace-induced bound state in the continuum. *Phys. Rev. Lett.* **118**, 166803 (2017).

47. Koshelev, K., Bogdanov, A. & Kivshar, Y. Meta-optics and bound states in the continuum. *Sci. Bull.* **64**, 836–842 (2019).
48. Kodigala, A. *et al.* Lasing action from photonic bound states in continuum. *Nature* **541**, 196 (2017).
49. Hsu, C. W., Zhen, B., Soljačić, M. & Stone, A. D. Polarization state of radiation from a photonic crystal slab. *ArXiv Prepr. ArXiv170802197* (2017).
50. Mandel, L. & Wolf, E. Coherence properties of optical fields. *Rev. Mod. Phys.* **37**, 231 (1965).

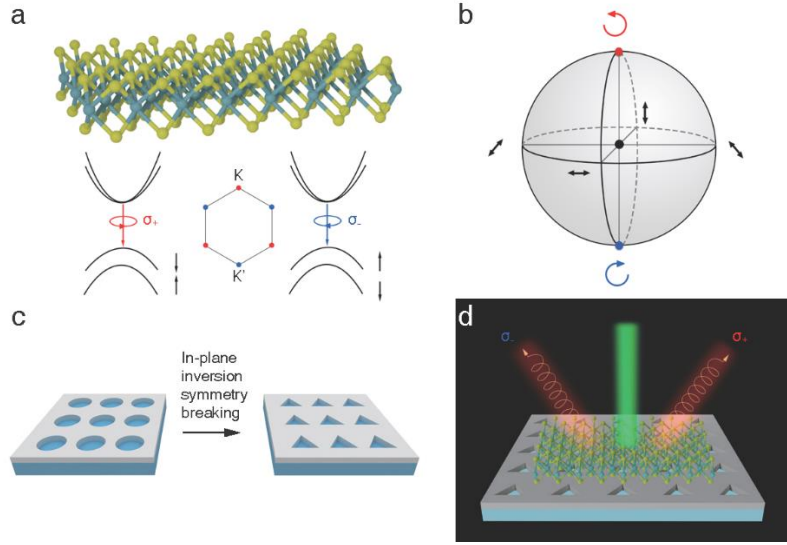


**Fig. 1 Schematics and principle.** **a** Schematic of WS<sub>2</sub> monolayer and optical selection rules at the K and K' valleys.  $\sigma_+$  ( $\sigma_-$ ) excitation corresponds to interband optical transition at the K (K') valley. **b** The normalized Poincaré sphere. Different azimuthal positions on the equator correspond to different linearly polarized states. Two poles correspond to two types of circularly polarized states. The center of the Poincaré sphere corresponds to vortex singularity. **c** PhC slabs with C<sub>4</sub> symmetry and with in-plane inversion symmetry broken. **d** Illustration of photoluminescence of WS<sub>2</sub> monolayer on the PhC slab with in-plane inversion symmetry broken. Valley photons with different chirality separate and radiate directionally in far field.

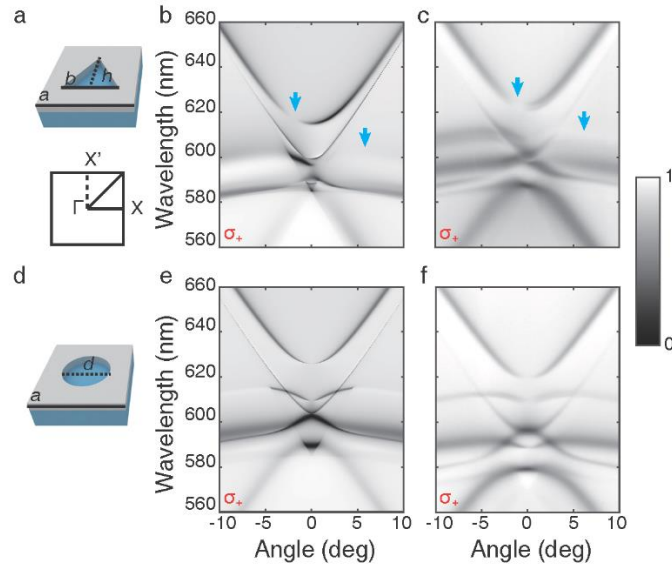


**Fig. 2 Simulated and experimentally measured angle-resolved transmittance spectra.** **a** Unit cell of photonic crystal slab with in-plane inversion symmetry broken. Triangle air holes are etched in the Si<sub>3</sub>N<sub>4</sub> layer. **b-c** Simulated and measured angle-resolved transmittance spectra in the visible range under  $\sigma_+$  polarized incidence. The incidence plane is along  $\Gamma$ -X direction. Diminished regions pointed out by blue arrows imply the existence of circularly polarized states after breaking the in-plane inversion symmetry. **d** Unit cell of photonic crystal slabs with in-plane inversion symmetry. Circle air holes are etched in the Si<sub>3</sub>N<sub>4</sub> layer. **e-f** Simulated and measured angle-resolved

transmittance spectra in the visible range under  $\sigma_+$  polarized incidence. The spectra is symmetric for the PhC slab with in-plane inversion symmetry.

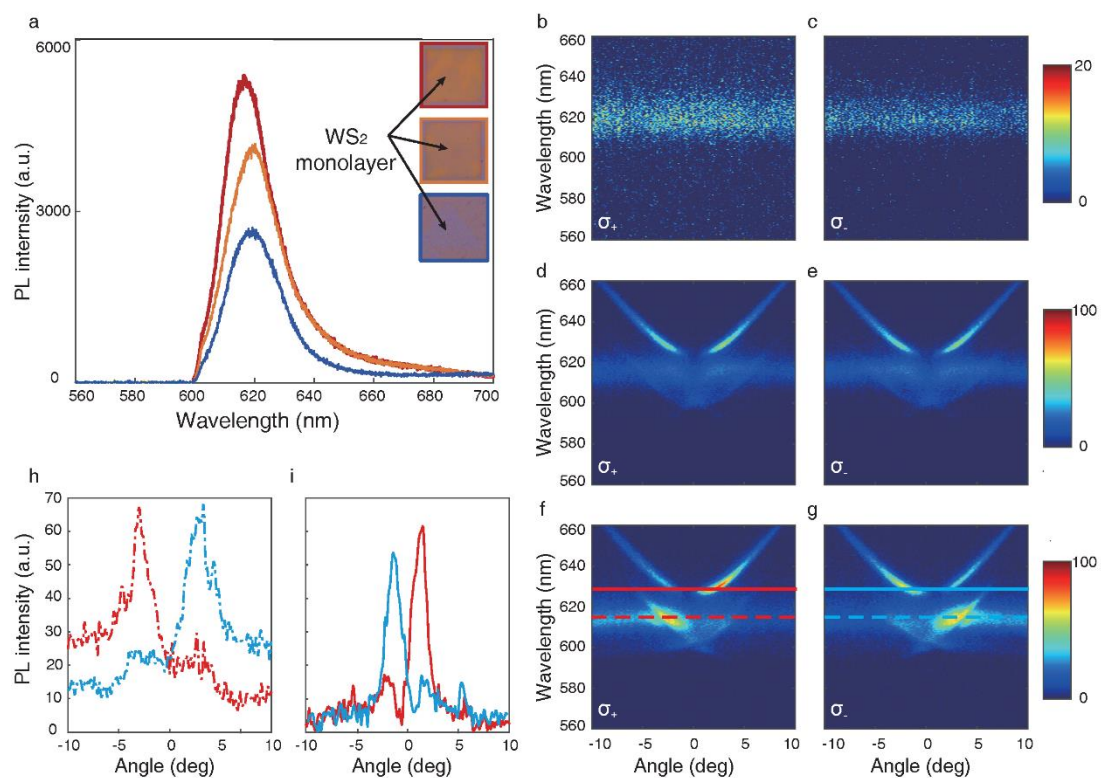


**Fig. 3 Angle-resolved PL spectra of WS<sub>2</sub> monolayer on different substrates at room temperature.** **a** Photoluminescence of WS<sub>2</sub> monolayer under linearly polarized light excitation. Red (orange) line corresponds to WS<sub>2</sub> monolayer on PhC slab without(with) in-plane inversion symmetry. Blue line corresponds to WS<sub>2</sub> monolayer on a flat substrate. The pumping light is 532 nm laser. **b-g** Angle-resolved PL spectra of WS<sub>2</sub> monolayer on three different substrates with  $\sigma_+$  ( $\sigma_-$ ) detection. The detection plane is along  $\Gamma$ -X direction. **h-i** Separation of  $\sigma_+$  (red) and  $\sigma_-$  (blue) polarized light at 615 nm (dot line) and 628nm (solid line) in **f-g**. The maximum  $P$  calculated is up to 84%.

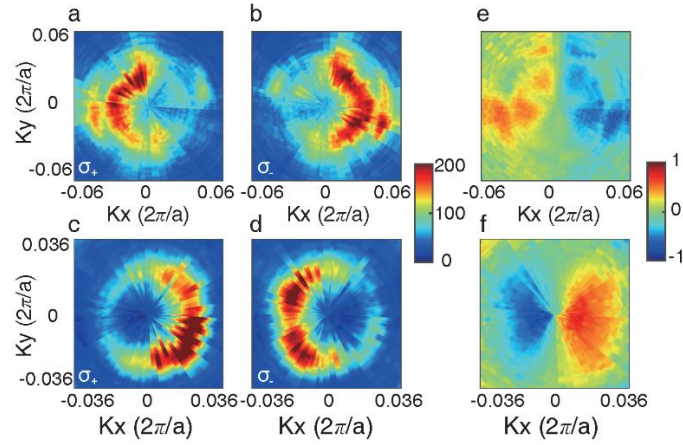


**Fig. 4 Experimental measurement of PL spectra and valley polarization in momentum space.** **a-d**  $\sigma_+$  and  $\sigma_-$  PL intensity distribution in momentum space at 615 nm (upper) and 628nm (lower). These are for WS<sub>2</sub> monolayer on the PhC slab with in-plane inversion symmetry broken. **e-f** Images of valley polarization  $P(k)$  in momentum space. The maximum  $P$  calculated is up to 88%.

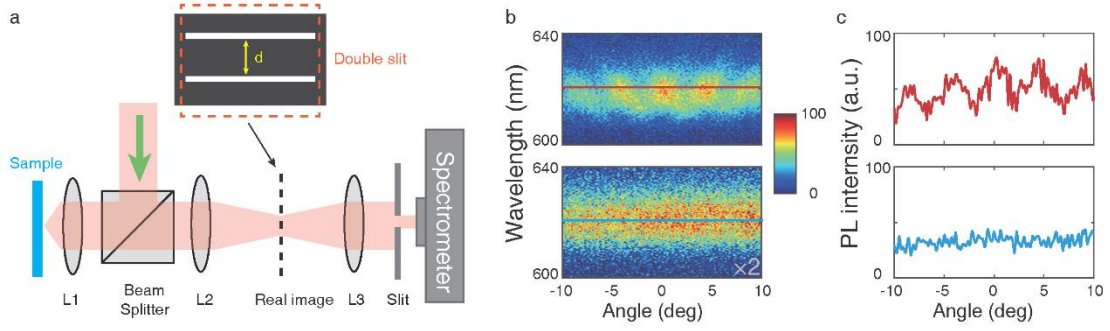


**Fig. 5 Experimental results of Young's double-slit interference.** **a** Schematic view of the experimental setup. L, Lens. The double-slit distance is  $d$ . The double slit is mounted on the real image plane. **b** The experimental results for the case of a 6 microns double-slit distance ( $d = 6$  microns). The upper is for WS<sub>2</sub> monolayer on PhC slab with in-plane inversion symmetry broken. The lower is for WS<sub>2</sub> monolayer on a flat substrate, with signal intensity shown twice the measurement. The detection plane is along  $\Gamma$ -X direction. **c** The interference intensity distribution in **b** at 621nm. The far-field emission of WS<sub>2</sub> monolayer on PhC slab with in-plane inversion symmetry broken has long-distance spatial coherence property.